ACS APPLIED ELECTRONIC MATERIALS

pubs.acs.org/acsaelm Article

# On the Contact Optimization of ALD-Based $MoS_2$ FETs: Correlation of Processing Conditions and Interface Chemistry with Device Electrical Performance

Reyhaneh Mahlouji, Yue Zhang, Marcel A. Verheijen, Jan P. Hofmann, Wilhelmus M. M. Kessels, Abhay A. Sagade, and Ageeth A. Bol*

Cite This: *ACS Appl. Electron. Mater.* 2021, 3, 3185−3199 Read Online

ACCESS | Metrics & More | Article Recommendations | Supporting Information

**ABSTRACT:** Despite the extensive ongoing research on $MoS_2$ field effect transistors (FETs), the key role of device processing conditions in the chemistry involved at the metal-to-$MoS_2$ interface and their influence on the electrical performance are often overlooked. In addition, the majority of reports on $MoS_2$ contacts are based on exfoliated $MoS_2$, whereas synthetic films are even more susceptible to the changes made in device processing conditions. In this paper, working FETs with atomic layer deposition (ALD)-based $MoS_2$ films and Ti/Au contacts are demonstrated, using current−voltage ($I$−$V$) characterization. In pursuit of optimizing the contacts, high-vacuum thermal annealing as well as $O_2$/Ar plasma cleaning treatments are introduced, and their influence on the electrical performance is studied. The electrical findings are linked to the interface chemistry through X-ray photoelectron spectroscopy (XPS) and scanning transmission electron microscopy (STEM) analyses. XPS evaluation reveals that the concentration of organic residues on the $MoS_2$ surface, as a result of resist usage during the device processing, is significant. Removal of these contaminations with $O_2$/Ar plasma changes the $MoS_2$ chemical state and enhances the $MoS_2$ electrical properties. Based on the STEM analysis, the observed progress in the device electrical characteristics could also be associated with the formation of a continuous $TiS_x$ layer at the Ti-to-$MoS_2$ interface. Scaling down the Ti interlayer thickness and replacing it with Cr is found to be beneficial as well, leading to further device performance advancements. Our findings are of value for attaining optimal contacts to synthetic $MoS_2$ films.

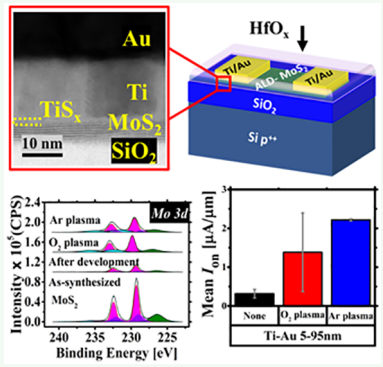


**KEYWORDS:** *$MoS_2$ FETs, atomic layer deposition (ALD), interface chemistry, Schottky contacts, plasma cleaning, current−voltage ($I$−$V$), XPS, STEM*

## INTRODUCTION

Atomically thin, all-surface, two-dimensional (2D) transition metal dichalcogenides (TMDCs) with electrical properties different from bulk materials have attracted significant interest in recent years for next generation nanoelectronic device schemes, beyond 10 nm complementary metal oxide semiconductor (CMOS) technology nodes.[1−3] TMDCs constitute a wide library of compounds, exhibiting diverse properties, ranging from semiconductors to (semi)metals and superconductors.[4,5]Among semiconducting TMDCs, $MoS_2$ is the most extensively studied material for electronic circuits and switches, specifically in the context of field effect transistors (FETs), owing to its outstanding electrical properties including a low subthreshold swing (~60 mV/dec),[6] $I_{on}/I_{off}$ ratios exceeding 10,[7−9] and reasonably high mobility values.[7,10] High degree of mechanical stability,[11,12] low variability,[13] and high reliability[8] as well as compatibility with conventional silicon CMOS fabrication process flows are other notable features of this material.[14−16] However, paving the way toward the implementation of 2D TMDCs as emerging materials into the mainstream CMOS platforms is not as straightforward as it appears to be. There are still several challenges that need to be addressed.

One of the critical issues is that 2D TMDC FETs, in general, are Schottky barrier transistors.[17] In other words, a potential barrier against the efficient carrier injection from the metal contacts toward the TMDC channel (due to their work function misalignments) is invariably formed, resulting in current rectification and high contact resistance ($R_c$) values.[18,19] In traditional bulk semiconductors, this issue is successfully resolved by using ion implantation, to heavily dope the regions below or around the contacts.[20] As a result, the metal work function is aligned with the semiconductor conduction band minimum ($E_c$), such that the carrier transport toward the

**Received:** April 23, 2021
**Accepted:** June 11, 2021
**Published:** June 28, 2021

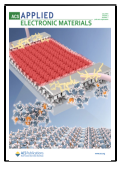

channel is facilitated with contacts becoming transparent (Ohmic). However, despite the ongoing research,[21,22] no such reliable and controllable doping technology for the 2D TMDC-based FETs, without damaging or perturbing the 2D layer properties, has been fully established yet.

In addition to the work function misalignment between the 2D TMDC and the contacts, the so-called Fermi levelpinning (FLP) phenomenon is the other contributor to the Schottky barrier and the high $R_c$.[23] Regardless of the metal choice and its work function value, it has often been observed that the $MoS_2$ FETs exhibit an *n*-type behavior, disobeying the Schottky−Mott model, where the barrier height for the electron injection is determined by the difference between the metal work function and the semiconductor electron affinity level.[24,25] The *n*-type observations are ascribed to the FLP at the metal-to-$MoS_2$ interface due to the combination of factors, including metal work function modulations as well as defect-/metal-induced gap state formations, which are most often energetically distributed in close proximity to $MoS_2$ $E_c$.[26] The origin of the gap states is strongly processing-related. These states could be intrinsic and formed at the time of layer growth (in the case of synthesized films)[27,28] or they could be induced during the device fabrication (e.g., when depositing metal contacts and when using lithographic processes for patterning).[29]

The majority of metals reacts with $MoS_2$, when brought into contact.[30] According to theoretical calculations, upon this interaction, the $MoS_2$ Fermi level ($E_F$) position shifts away from its intrinsic level, denoting that $MoS_2$ becomes doped at the contact regions.[31] Inert metals, such as Au, exhibit weak van der Waals (vdW) interactions, whereas more chemically reactive metals (such as Ti and Cr) form covalent bonds with the underlying $MoS_2$ and disrupt the $MoS_2$ electronic band structure.[31,32] In case the formation energy of metal-to-sulfur (Ti−S, Cr−S) is less than the formation energy of molybdenum-to-sulfur (Mo−S),[33] a sulfur-deficient $MoS_2$ forms at the interface upon metal deposition.[26] Apart from the metal choice, it has been experimentally observed that the chemical compound formed at the metal-to-$MoS_2$ interface strongly depends on the metal deposition conditions.[34,35] For example, McDonnell et al.[35] have demonstrated that when a Ti contact is deposited on $MoS_2$ at high vacuum (HV) (pressure $>10^{-6}$ mbar), Ti is likely to react with oxygen and form $TiO_x$ at the interface, owing to the background oxygen present at such pressures. On the other hand, for ultrahigh vacuum (UHV) environments (pressure $<10^{-9}$ mbar), Ti shows a stronger reaction with the underlying $MoS_2$, resulting in the formation of Ti−S bonds at the interface[35] and disruption of the semiconducting layer beneath as well as its electronic band structure,[31,36] leaving behind gap states mainly of Mo character.[26,31,36] Several efforts have been made in recent years to control the gap state formation. Insertion of ultra thin interfacial layers of oxides such as $Ta_2O_5$,[37] $Al_2O_3$,[38] and $TiO_2$[38,39] at the interface was overall beneficial in mitigating the impact of the deposited metal on the $MoS_2$ layer beneath. This has in most of the cases led to Fermi level de-pinning, Schottky barrier height lowering and $R_c$ reduction for the $MoS_2$ FETs. Similarly, when growing the Ti metal in a HV environment, the inevitable formation of interfacial $TiO_x$, as a barrier layer against the direct metal interaction with $MoS_2$, has positively influenced the transport properties.[29] These studies altogether indicate that connecting the interface chemical reactions with the processing conditions is vital for appropriately understanding the electrical behavior of the $MoS_2$ FETs, a perspective that should not be overlooked or underestimated.

It is also commonly known that the process of device fabrication can itself induce additional impurities and defects in the contact areas. In a standard device fabrication flow, where the contacts are defined by means of lithographic and patterning processes, the opened areas intended for the contacts may not always be fully cleaned from the resist residues. The presence of these contaminants can subsequently lead to low-quality contacts.[29] In conventional CMOS process flows, a plasma cleaning step is usually followed after the development step to ensure a complete resist removal.[20] This cleaning treatment is reckoned to be a harsh process for $MoS_2$ films, often creating additional defects or forming other compounds on their surface.[40] Nonetheless, it has been reported that a mild and short $O_2$ plasma cleaning step can effectively eliminate the resist residues without damaging the $MoS_2$ lattice, leading to noninterrupted contacts, and thus improved electrical performance.[29] $H_2$ plasma and a subsequent usage of carbonyl disulfide have also been shown to clean and restore the 2D film properties.[41]

High-temperature post deposition annealing is another standard technique in industry for mitigating the impurities and defects at the metal-to-semiconductor interfaces.[20] However, for $MoS_2$ FETs, this treatment resulted in contradictory outcomes. Some groups observed performance enhancements,[42,43] whereas others reported deteriorations in electrical features.[7,44] These inconsistencies originate from the chemical interactions at the metal-to-$MoS_2$ interface that can create/annihilate defects, re-emphasizing that the $MoS_2$ FETs are defect-mediated systems. Therefore, the relation between the processing conditions, the interface chemistry, and the device electrical performance has to be independently investigated for every device fabrication process flow.

It is also noteworthy that the majority of the abovementioned studies have been conducted on exfoliated $MoS_2$, whereas the role of intrinsic and process-induced defects in transport properties at the contact sites can be even more pronounced for synthetic $MoS_2$ films.

In this work, atomic layer deposition (ALD) is employed for the growth of $MoS_2$ films. Although chemical vapor deposition (CVD) is still the preferred synthesizing technique to achieve the best quality 2D TMDCs in large areas,[10,45,46] in the quest of Ångstrøm level thickness control and highly conformal layers (suitable for 3D structures) while maintaining a low thermal budget, required for industry processes, ALD has also been gaining attention in recent years.[47−50] We comprehensively study the impact of device processing conditions on the chemistry involved at the metal-to-$MoS_2$ interface and connect the two to the current−voltage ($I$−$V$) results, obtained from electrically characterizing the fabricated FETs, with ALD-based $MoS_2$ films and Ti/Au contacts. In pursuit of optimizing the contacts to our $MoS_2$, we investigate the influence of thermal annealing and plasma cleaning the contacts (with $O_2$ and Ar) on the overall device electrical performance while scaling down the Ti interlayer thickness. We relate the observed $I$−$V$ characteristics to the interface chemistry, using X-ray photoelectron spectroscopy (XPS) and cross-sectional scanning transmission electron microscopy (STEM) analyses. Furthermore, the impact of changing the contact metal type will be discussed. Our findings shed light on the path toward a better understanding of the interface chemistry as well as the carrier transport in ALD-


https://doi.org/10.1021/acsaelm.1c00379
ACS Appl. Electron. Mater. 2021, 3, 3185−3199

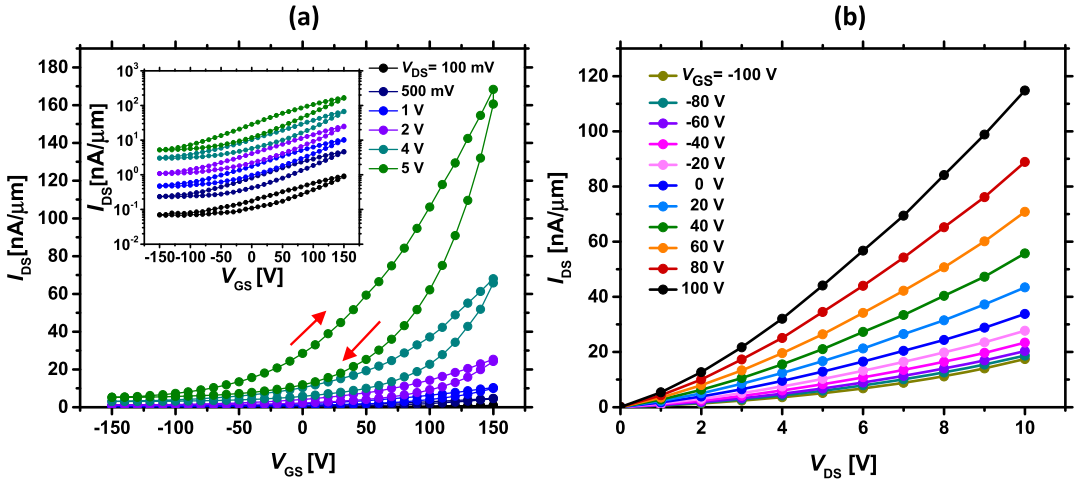


**Figure 1.** (a) Double sweep transfer curves of the ALD-based $MoS_2$ FET, for different lateral fields, on a linear scale (the red arrows indicate the direction of forward and backward sweeps). The inset shows a semilog plot, for better visualizing the current change with $V_{DS}$ in the off-state regime. (b) Forward sweep output $I_{DS}-V_{DS}$ characteristics for different $V_{GS}$ values.

based $MoS_2$ FETs and their strong reliance on the device processing conditions.

## EXPERIMENTAL SECTION

**$MoS_2$ Film Synthesis.** For this study, multilayer $MoS_2$ films with a thickness of about 3.6 nm (7−8 monolayers) were synthesized using a two-step approach, where plasma-enhanced ALD was employed for the large-area and thickness-controlled growth of $MoO_x$ on a commercial ALD reactor from Oxford instruments (FlexAL). Then, the as-deposited $MoO_x$ films were annealed in a $H_2S$ environment, with 10% $H_2S$/90% Ar, at 900 °C, for 45 min, to eventually obtain multilayer $MoS_2$. Further details of the film synthesis are published in our previous work by Sharma et al.[51] In all cases, the growth took place on degenerately doped ($p^{++}$) silicon substrates with ∼285 nm thermal $SiO_2$, acting as global back-gates for the fabricated $MoS_2$ FETs.

**Fabrication of Back-Gate $MoS_2$ FETs.** The back-gate $MoS_2$ FETs were fabricated by the common electron beam lithography (EBL) patterning technique. For this purpose, a polymer resist (950K PMMA A4) was spin-coated on the as-synthesized $MoS_2$ films, with a spin speed of 4000 rpm, for 60 s. After baking poly(methyl methacrylate) (PMMA) at 180 °C, for 5 min, a contact layout design was transferred on it by an EBL exposure, using a commercial RAITH micrograph system (EBPG5150). Upon developing the patterned PMMA with an organic developer [methyl isobutyl ketone (MIBK)/isopropyl alcohol (IPA) mixture with a 1:3 ratio], the contact windows (source and drain regions) were opened. The development step was then followed by the deposition of 20/80 nm of Ti/Au on $MoS_2$, using an e-beam evaporator, operated at room temperature, with a base pressure of $\sim 4 \times 10^{-7}$ mbar and a deposition rate of 1 Å/s. Subsequently, contacts were delineated by a lift-off process in an acetone solvent, where the PMMA together with the deposited metal were removed from the nonexposed regions. For defining the $MoS_2$ channel regions and isolating the individual $MoS_2$ devices, a second lithography step (to transfer a relevant overlay pattern onto the samples) was employed. After this exposure and the PMMA development, $MoS_2$ was dry-etched from the opened areas, in a reactive ion etching (RIE) reactor (GP-RIE, Oxford Instruments), using $SF_6/O_2$ plasma at room temperature, with a flow rate of 16/4 sccm, for 20 s, at a pressure of 22.5 mTorr and a forward power of 25 W. Then, the PMMA layer (which was protecting the channel regions during the plasma etching process) was removed in acetone. Finally, 30 nm of $HfO_x$ (high-$\kappa$) was grown on the fabricated $MoS_2$ FETs, using PE-ALD[52] at 100 °C (FlexAl ALD reactor, Oxford Instruments). The $HfO_x$ deposition is mainly for capping the fabricated devices and screening the charge impurity scatterings as one of the major mobility-limited mechanisms for $MoS_2$ channels.[53] The optical microscopic top view image of the as-fabricated $MoS_2$ FETs and the final device schematic cross section are provided in our Supporting Information (see section S.1).

**Annealing the $MoS_2$ Contacts.** Investigating the impact of annealing the contacts on the electrical performance of the ALD-based $MoS_2$ FETs, the fabricated devices were vacuum annealed at 300 °C, for 2 h, at a base pressure of $\sim 7 \times 10^{-6}$ Torr (HV), in the ALD reactor and prior to the $HfO_x$ deposition step.

**Plasma Cleaning the Contact Openings on $MoS_2$.** To efficiently remove the possibly existing organic residues from the surface of our $MoS_2$ films, a mild plasma cleaning step right before the contact deposition step with two different gases ($O_2$ and Ar) was examined. The plasma cleaning conditions were kept similar for both gases, being introduced into the chamber with a flow rate of 20 sccm, for 5 s, at a pressure of 200 mTorr and using a plasma power of 50 W.

**Scaling Down the Ti Interlayer Thickness.** Evaluating the influence of the Ti interlayer on the overall device electrical performance, various Ti thicknesses in the range of 20 nm down to 2.5 nm were examined while retaining the whole Ti/Au contact stack thickness at 100 nm. A complete Ti removal was also inspected. For all the cases, the evaporation conditions were constant (a base pressure of $\sim 4 \times 10^{-7}$ mbar and a deposition rate of 1 Å/s).

**Replacement of Ti/Au with Cr/Au.** For further optimizing the contacts to our $MoS_2$ films, the Ti interlayer was replaced with Cr. The Cr evaporation took place in the same chamber and under the similar conditions to those of the Ti case (a base pressure of $\sim 4 \times 10^{-7}$ mbar and a deposition rate of 1 Å/s).

**Electrical Characterization.** The electrical performance of the fabricated $MoS_2$ FETs was evaluated by characterizing their room temperature $I-V$ response. In all the cases, the measurements were conducted on 500 nm long and 1 $\mu$m wide $MoS_2$ channels. The setup used for this purpose was a cryogenic probe station (Janis ST-500) with a base pressure of $\sim 1.9 \times 10^{-4}$ mbar, connected to a Keithley 4200-SCS parameter analyzer.

**Surface Characterization.** Correlating the electrical characterizations with the surface chemistry, ex situ XPS was performed on the $MoS_2$ surface after its synthesis, contact pattern development, and plasma cleaning treatments, with both Ar and $O_2$ gases. For this purpose, a Thermo Scientific K-alpha KA1066 spectrometer (Thermo Fisher Scientific, Waltham, MA) with a monochromatic Al K$\alpha$ X-ray radiation source ($h\nu$ = 1486.6 eV) was utilized. The measurements were carried out with an X-ray beam spot size of 200 $\mu$m, at a take-off angle of 60° and a pass energy of 50 eV, combined with an electron flood gun, to efficiently neutralize the existing charges on the samples as well as to correct for the nonuniform and differential charging. The acquired spectra were later chemically quantified and deconvoluted with Avantage software. All the peaks were also further binding energy calibrated with respect to the C 1s adventitious carbon peak (284.8 eV).


https://doi.org/10.1021/acsaelm.1c00379
ACS Appl. Electron. Mater. 2021, 3, 3185−3199

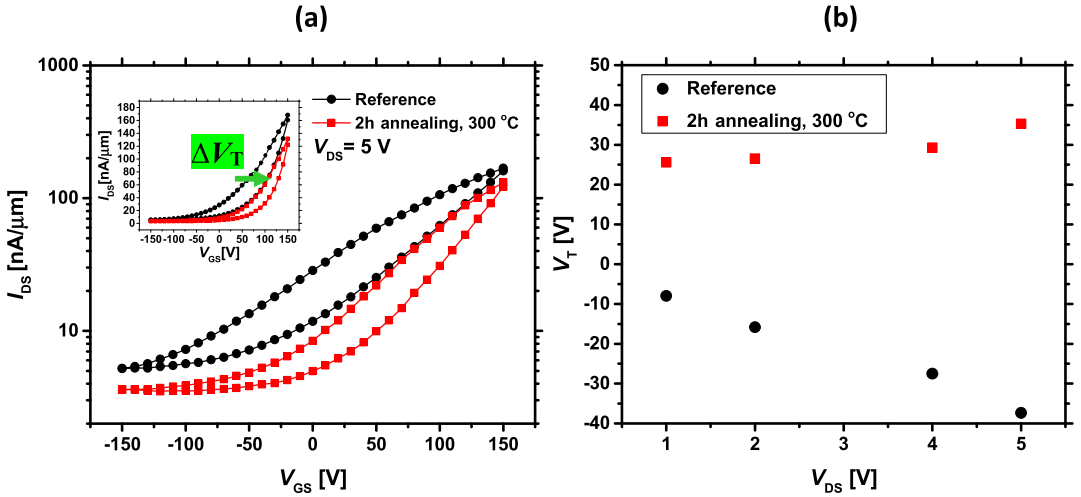


**Figure 2.** (a) Transfer curves of the annealed and the nonannealed cases, on a semilog scale (the inset shows the plot with a linear scale, and the green arrow indicates the positive shift of $V_T$ upon the annealing treatment). (b) Forward sweep $V_T$ and its dependence on $V_{DS}$ for both the annealed and the nonannealed devices.

**Structural Characterization.** The microstructure of the metal-to-$MoS_2$ interface was investigated using cross-sectional STEM analysis, conducted using a JEOL ARM 200F operated at 200 kV. The sample that received $O_2$ plasma cleaning treatment, prior to the contact deposition, was selected for this evaluation. The common lift-out procedure with focused ion beam (FIB) was followed to prepare an imaging specimen on a Mo support grid. A Mo grid was chosen rather than a Cu grid, as previous studies have shown that redeposited Cu by the FIB process can react with the sulfur in $MoS_2$, creating undesirable $CuS_x$ precipitates on the transmission electron microscopy (TEM) specimen surface. Prior to the so-called FIB milling step, the contact stack was covered with a protective layer of $SiO_2$ and Pt, using electron beam-induced deposition (EBID) and ion beam-induced deposition (IBID), respectively.

## RESULTS AND DISCUSSION

Throughout the Results and Discussion section, the reference sample is represented by the ALD-based $MoS_2$ FET with a 3.6 nm thick, 1 $\mu$m wide, and 500 nm long $MoS_2$ channel and 20/80 nm of Ti/Au contacts (no plasma cleaning of the contact areas or post annealing treatments). The device shows typical transfer curves ($I_{DS}$–$V_{GS}$) with dual sweep (Figure 1a) and output curves ($I_{DS}$–$V_{DS}$) (Figure 1b). As can be seen from Figure 1a, the fabricated device exhibits *n*-type characteristics with the maximum drain current ($I_{on}$) reaching 180 nA/$\mu$m, at $V_{GS}$ = 150 V and the highest applied lateral field of $V_{DS}$ = 5 V. The minimum current ($I_{off}$) (at $V_{GS}$ = −150 V) is few nA/$\mu$m for all the $V_{DS}$ values (see the semilog plot shown as the inset) and does not decrease monotonically with more negative $V_{GS}$. The latter is due to the dielectric encapsulation effect and suppression of hole contribution, which is observed in other related studies as well.[54,55] In addition, the hysteresis and, hence, the threshold voltage ($V_T$) of both backward and forward sweeps show strong dependence on the applied $V_{DS}$ (apart from the their general dependence on $V_{GS}$). All these observations indicate that more than one phenomenon is contributing to the $MoS_2$ charge transport. Some of the causes can be listed as follows: defect states at the contact-to-$MoS_2$ interface, $MoS_2$ structural defects (grain boundaries and dislocations) and defect states/charged trapping sites at the dielectric-to-$MoS_2$ interface as well as high $R_c$.

Hysteresis usually increases with $V_{GS}$ and is weakly affected by $V_{DS}$. However, in our study, the hysteresis increases with $V_{DS}$, indicating a profound influence of defects and trapping of carriers inside the $MoS_2$ lattice. The nonlinearity in the output characteristics (shown in Figure 1b) is also due to Schottky barrier formation between $MoS_2$ and the contacts. Recent reports from several researchers have shown that all the abovementioned effects are responsible for $V_T$ dependence on $V_{DS}$.[8,29,56−58] Therefore, further studies are followed to tailor the contacts and to investigate the influence of different processing conditions, with the aim of improving the device electrical performance.

**Annealing the ALD–$MoS_2$ Contacts.** As mentioned earlier, annealing the contacts is a common practice in conventional CMOS process flows to improve the electrical performance, through reducing the density of defects at the metal-to-semiconductor interfaces and eliminating the surface charges from the semiconducting channel regions.[20] However, inclusion of this step and its impact on the overall device electrical characteristics have not yet been studied for ALD-based $MoS_2$ FETs with Ti/Au contacts. To investigate that, the fabricated devices were thermally HV annealed at 300 °C, for 2 h and prior to the $HfO_x$ (high-$\kappa$ dielectric) deposition. Figure 2a compares the transfer curves of a nonannealed (reference) sample versus the annealed one at $V_{DS}$ = 5 V, on a semilog scale. For both cases, the Ti/Au contacts were 20/80 nm thick. As can be seen from the plot, upon the HV annealing treatment, $I_{on}$ does not improve, whereas $I_{off}$ slightly drops. In addition, $V_T$ shifts from negative to positive values for both back and forward sweeps. The latter is more evident on a linear scale, provided as the inset of Figure 2a. These observations certainly imply that when the HV annealing treatment is employed, the chemical state at the Ti-to-$MoS_2$ interface changes, but not in favor of improving the device on-state performance. The reduction in $I_{on}$ could be explained by the interdiffusion of the elemental compounds (Ti, Mo and S), which is facilitated at elevated temperatures. As a result, a disordered and an intermixed region would be formed at the Ti-to-$MoS_2$ interface, as has previously been verified for the annealed Ti contacts to the exfoliated $MoS_2$ films.[59] Furthermore, the annealing process in this study is performed in a HV chamber. The presence of background water and/or oxygen and its possible reaction with the $MoS_2$ surface at the channel regions, as well as the Ti-to-$MoS_2$ interfaces (from the Ti edge sites), may lead to the formation of oxide-containing


https://doi.org/10.1021/acsaelm.1c00379
ACS Appl. Electron. Mater. 2021, 3, 3185−3199

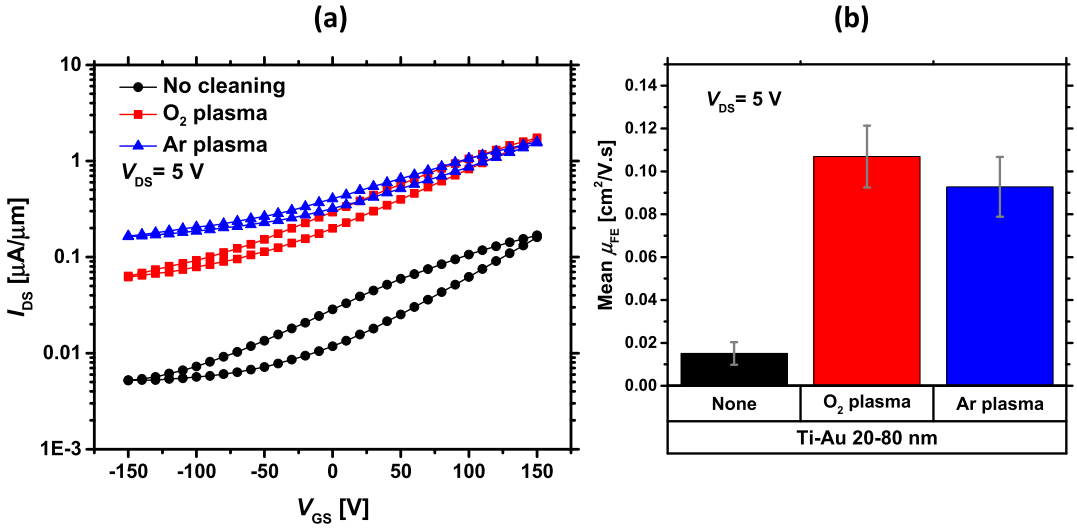


**Figure 3.** (a) Impact of the $O_2$ and Ar plasma cleaning treatments (prior to the contact deposition) on the device electrical performance. (b) Average extracted maximum FE mobility values for all the three cases of study.

compounds, all of which could impede the enhancements in the device on-state.

Further elaborating the discussion, $V_T$ values of the reference and the annealed samples are extracted and compared in Figure 2b. The data are derived using the Y-function method[60] (See the Supporting Information, Section S.2 for details of the extraction method). Considering the reference sample, modulation of the drain current (by changing $V_{DS}$) results in shifting $V_T$ toward more negative values (from −8 to −37 V). As mentioned before, this indicates that the defect states (at the contact-to-$MoS_2$ and/or the oxide-to-$MoS_2$ interface) dope $MoS_2$ to the *n*-type and contribute to the current. However, the annealed device shows a completely reversed behavior. As $V_{DS}$ increases, $V_T$ shifts to more positive values (from +25 V to +35 V). The positive shift of $V_T$ with increasing $V_{DS}$ together with the observed reduction in $I_{off}$ suggest that the defect density close to $E_c$ of $MoS_2$ decreases and that $MoS_2$ becomes relatively less *n*-type doped upon the annealing treatment. Moreover, the inset of Figure 2a shows that the hysteresis reduces after this process, inferring the defect density mitigation at the oxide-to-$MoS_2$ interface. All these observations are pointing toward a direction that a portion of the conduction in the $MoS_2$ FETs is carried out by the defect states (as formerly also suggested by McDonnell et al.[61]), such that by annealing the contacts, the influence of these states become quite less pronounced.

Figure 2b also reveals that for all the $V_{DS}$ values, the overdrive voltage ($V_{ov} = V_{GS} - V_T$) does not drop below 100 V (at $V_{DS} = 5$ V, $V_{ov} = 150$ V − 35 V (annealed case) or $V_{ov} = 150$V + 37 V (reference case)). Therefore, our devices work in the linear operating regime.

**$O_2$ and Ar Plasma Cleaning of the Contact Openings.** Further optimizing the contacts for our $MoS_2$ FETs, the effect of plasma cleaning, prior to the metal contact deposition, is assessed in this Section. As discussed earlier, upon using PMMA (or any other polymer resist) for patterning the contacts with EBL, traces of the resist may contaminate the opened areas, subsequently causing formation of discontinuous contacts to $MoS_2$ and affecting the overall device electrical performance. Marinov et al.[41] have recently reported that $H_2$ plasma treatment at 300 °C is highly effective in clearing their synthetic $WS_2$ surface from organic residues. They exclusively highlighted that the cleaning process has to be performed at sufficiently high temperatures to impose the least damage to the 2D lattice. In a former effort, Bolshakov et al. also suggested inclusion of a room temperature plasma step, to clean up the surface of their exfoliated $MoS_2$, prior to the contact deposition.[29] Therefore, to efficiently remove the possibly existing residual components from the surface of our ALD-based $MoS_2$ films, we examined a mild and short plasma cleaning step at room temperature, right before the contact deposition, with $O_2$ and Ar plasma sources, which are regularly employed in microfabrication. The plasma parameters (time, flow rate, power, and pressure) were initially optimized on a blanket $MoS_2$ film for the $O_2$ gas source. Then, to allow for direct comparison, these conditions were kept similar for both $O_2$ and Ar. Here, we also note that performing the cleaning process at 300 °C (as suggested by Marinov et al.[41]) is not applicable in our study because PMMA evaporates at such high temperatures, while it needs to remain for the contact delineation step. After the plasma exposures, Ti/Au contacts were deposited with a similar thickness and evaporation conditions to those of the reference sample.

***I*–*V* Analysis.** Figure 3a demonstrates the transfer characteristics of the samples that have been treated with the $O_2$ and Ar plasmas and compares their behavior with respect to the uncleaned (reference) sample, at $V_{DS} = 5$ V. As can be seen, employing both the $O_2$ and Ar plasmas, prior to the contact deposition, has been effective in improving the on-state performance, with increasing $I_{on}$ up to one order of magnitude and reaching nearly 1.5−2 $\mu$A/$\mu$m. Hence, the average maximum field effect (FE) mobility, extracted from measuring various devices (typically three to four devices), has improved six to eight times (Figure 3b). See the Supporting Information, Section S.3 for the mobility extraction technique. Despite the significant enhancement in $I_{on}$ as well as the mobility, $I_{off}$ increases, and $V_T$ shifts more negatively (from −37 V for the reference case to −42 V for the $O_2$ plasma case and to −70 V for the Ar plasma case), both indicating that the $MoS_2$ channel is degenerately *n*-type doped after the plasma cleaning processes. As a consequence of this excess carrier concentration, the back-gate oxide is unable to fully deplete the channel and fails to efficiently modulate the drain current. However, the increase in $I_{off}$ for the $O_2$ plasma case is less severe than when the Ar plasma-


https://doi.org/10.1021/acsaelm.1c00379
ACS Appl. Electron. Mater. 2021, 3, 3185−3199

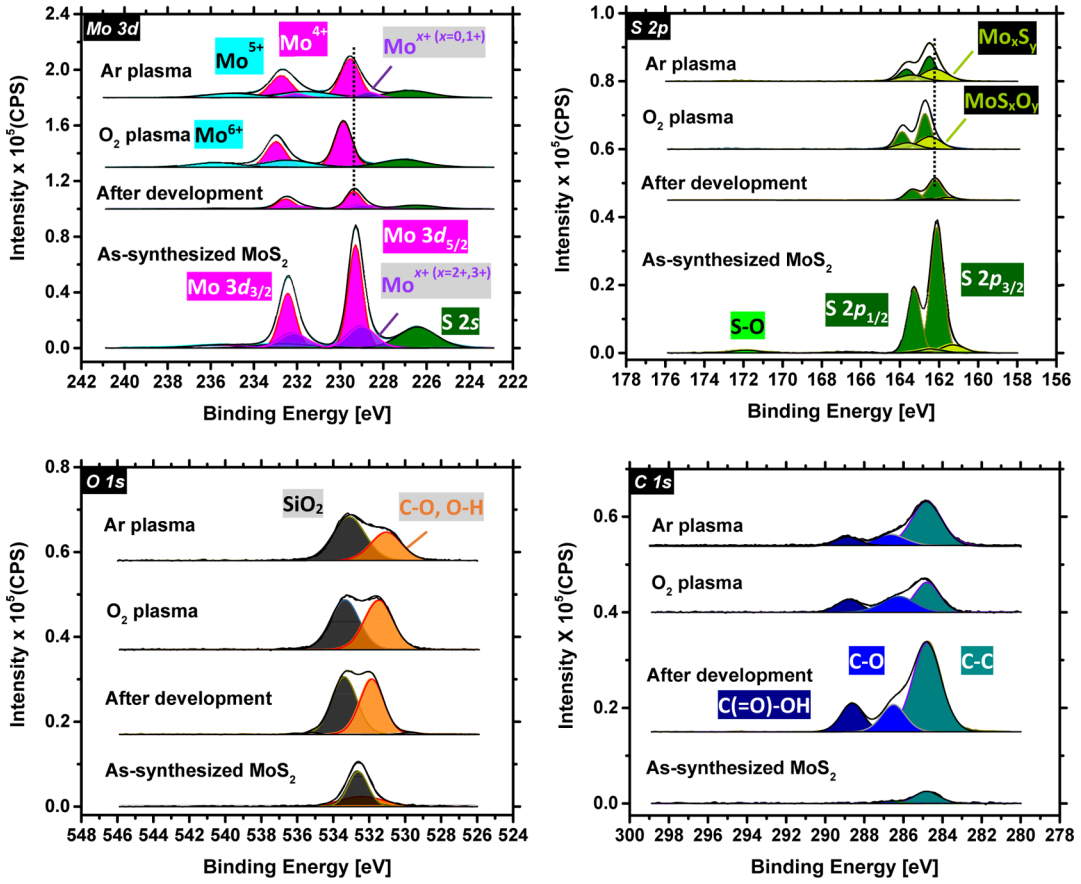


**Figure 4.** Mo 3d, S 2p, O 1s, and C 1s core level spectra of the as-synthesized $MoS_2$, after the contact pattern development and after the different plasma cleaning treatments (offset vertically).

treated sample is considered. This suggests different chemical interactions at the metal-to-$MoS_2$ interface, based on the plasma being utilized.

**XPS Analysis.** Bridging the $I-V$ characterization to the chemistry involved at the metal-to-$MoS_2$ interface, ex-situ XPS analysis was performed on the $MoS_2$ surface, after its synthesis, contact pattern development, and cleaning treatments, with both the $O_2$ and Ar plasmas. Figure 4 shows the acquired elemental data from the XPS measurements for the core level spectra of the Mo 3d, S 2p, O 1s and C 1s, binding energy calibrated with respect to the C 1s $sp^3$ component of the adventitious peak, set to 284.8 eV. The very bottom panel in each plot corresponds to the as-synthesized $MoS_2$ film, prior to the EBL patterning and any processing treatments. The rest of the panels are offset vertically. After fitting and deconvoluting the peaks, the Mo 3d core level spectrum of the as-synthesized $MoS_2$ shows two major peaks at 229.2 and 232.4 eV, representing the Mo $3d_{5/2}$ and Mo $3d_{3/2}$ binding energies for the $Mo^{4+}$ oxidation state ($MoS_2$), respectively. Two minor peaks with a slight shift to relatively lower binding energies at 228.9 and 232.1 eV are also discernible. These peaks are attributed to lower oxidation states, $Mo^{x+}$ ($x$ = 2+, 3+), suggesting that our $MoS_2$ film is substoichiometric/sulfur-deficient, intrinsic to its synthesis route.[62] Furthermore, as a result of the S 2s core level overlapping with the Mo 3d spectrum, an additional peak at 226.3 eV is discernible. Minor Mo components with oxidation states other than 4+ are also detected at higher binding energies, inferring that the surface of our synthetic $MoS_2$ film contains a slight amount of oxidized species ($MoO_x$), upon its exposure to the ambient air. Evaluating the S 2p spectrum, signatures of the S $2p_{3/2}$ and S $2p_{1/2}$ core levels are detected at 162.0 and 163.2 eV, respectively. In addition, an extra peak is found at higher binding energies (171.8 eV) related to the S−O compound formation, reflecting $MoS_2$ surface oxidation. As far as the O 1s and C 1s core level spectra are concerned, no specific chemical state, other than the adventitious oxygen and carbon, in the forms of C−O, O−H and C−C, can be distinguished. For better viewing these peaks, they are separately provided in the Supporting Information, Section S.4.

After defining the contact areas with EBL and PMMA development in MIBK/IPA solution, the binding energies for both the Mo 3d and S 2p peaks shift +0.1 eV, indicating that the $MoS_2$ chemical state might have been changed and that its $E_F$ position displaced +0.1 eV closer to $E_c$, upon the development process.[29] In addition, the O 1s and C 1s spectra clearly demonstrate the presence of new organic compounds of C−O and O−H nature, with binding energies located at 531.8 eV in the O 1s spectrum and at 286.4 and 288.5 eV in the C 1s spectrum, respectively. As can be seen, the presence of these residual species on the $MoS_2$ surface leads to a significant peak intensity drop in the Mo 3d and S 2p core level spectra, relative to the as-synthesized case. For better visualization, the as-mentioned spectra are separately provided in the Supporting Information, see Section S.5. The observed shift in the $MoS_2$ binding energies together with the detection of organic compounds on the $MoS_2$ surface comprehensively pinpoint that after the development step, residues of the resist material (PMMA) are still present on the $MoS_2$ surface. Therefore,


https://doi.org/10.1021/acsaelm.1c00379
ACS Appl. Electron. Mater. 2021, 3, 3185−3199

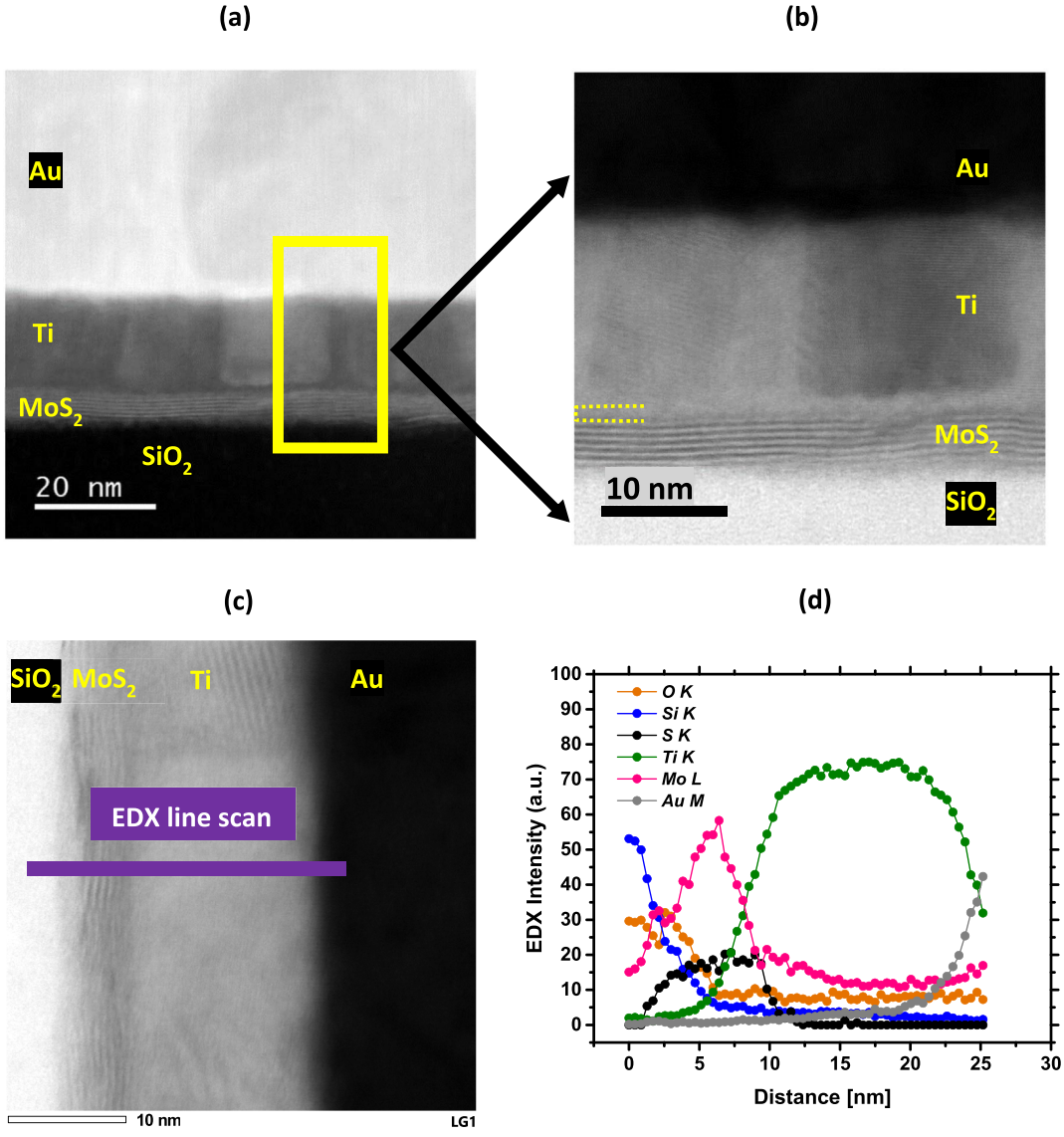


**Figure 5.** (a) Cross-sectional HAADF STEM image of the $O_2$ plasma-treated $MoS_2$ contact stack, (b) higher-resolution ABF−STEM image of the contact stack, to better visualize the interlayer between the $MoS_2$ and Ti (the yellow dashed lines determine the interlayer region), (c) HAADF image displaying the location of the EDX−STEM line scan, highlighted by the purple line and (d) compositional profile along the distance of the EDX line scan.

utilization of the developer solution (MIBK/IPA) alone may not be sufficient to completely remove the PMMA from the opened areas on the $MoS_2$ surface. This non-negligible concentration of organic impurities could be considered as one of the main sources of changes in the $MoS_2$ chemical state and its $E_F$ position.[29]

Applying a mild and short $O_2$ plasma, the peak intensities in both the C 1s and O 1s spectra drop, and their full width at half-maximum (FWHM) increase, compared with the former case, where the PMMA residual components were still considerable on the $MoS_2$ surface. Hence, the cleaning process is effective in removing at least a part of the residues from the $MoS_2$ surface, leading to peak intensity enhancements in both the Mo 3d and S 2p core level spectra. The binding energies for both the Mo 3d and S 2p major peaks are also shifted +0.5 eV after the $O_2$ plasma treatment, implying that the $MoS_2$ $E_F$ position is shifted +0.5 eV closer to $E_c$ as well (relative to the as-developed case). In addition to the $E_F$ displacement, an extra doublet appears in the Mo 3d core level spectrum with peak positions of 232.4 and 235.7 eV, attributed to the $Mo^{6+}$ oxidation state ($MoO_3$). Meanwhile, in the S 2p spectrum, fingerprints of other oxidized species (e.g. $MoS_xO_y$) become more pronounced,[35] with peak positions located at 162.4 and 163.5 eV. All these findings indicate that the surface of $MoS_2$ is slightly oxidized upon the $O_2$ plasma cleaning process.

Finally, Ar plasma is examined for removing the organic residues. Upon this treatment, the peak intensities pertaining to the residual organics in the O 1s and C 1s spectra further reduce, and their FWHM increase accordingly. This comparison is with respect to the previous case of study, implying that the application of Ar plasma is more efficient than that of $O_2$ plasma in cleaning the $MoS_2$ surface from the resist contaminations. As far as the Mo 3d and S 2p core levels are concerned, the peak positions in both spectra shift +0.2 eV, relative to the as-developed case, as an indication of the $E_F$ shift toward $E_c$ with the same magnitude. Unlike the $O_2$ plasma treatment, in the Mo 3d spectrum, two minor peaks corresponding to lower oxidation states [$Mo^{x+}$ ($x$ = 0, 1+)]


https://doi.org/10.1021/acsaelm.1c00379
ACS Appl. Electron. Mater. 2021, 3, 3185−3199

appear upon the surface exposure to the Ar plasma. The presence of these oxidation states can be attributed to the preferential sputtering of sulfur when Ar plasma is employed, leaving behind Mo states of mostly metallic nature. Sulfur sputtering is also evident when considering the S 2p core level spectrum and the decreased binding energies for the minor peaks, as a sign of sulfur-deficient $Mo_xS_y$ species.[35] On the other side of the Mo 3d spectrum (higher binding energies), minor components of the $Mo^{5+}$ state occur as well. This indicates that the sulfur-deficient $MoS_2$ surface is slightly oxidized, likely due to the background oxygen present inside the chamber during the Ar plasma cleaning or the sample exposure to the ambient air after the process.

**STEM Analysis.** To further investigate the chemical species formed at the metal-to-$MoS_2$ interface and its influence on the device electrical performance, a cross-sectional STEM analysis was performed for the $MoS_2$ FETs that received $O_2$ plasma cleaning treatment, prior to the metal deposition. Figure 5a shows a high-angle annular dark field (HAADF)−STEM image of the Au/Ti/$MoS_2$ contact stack. At the interface between Ti and $MoS_2$, an extra interlayer with a different contrast than Ti and $MoS_2$ can be clearly distinguished. A higher-resolution STEM image, obtained in annular bright field (ABF) mode, provided in Figure 5b, reveals that this interlayer is amorphous and evenly distributed along the interface with a thickness of about 2 nm. Because the $MoS_2$ surface is initially exposed to the $O_2$ plasma, it is expected that organic residues do not play a significant role in the formation of such an interlayer.

For exploring the compositional distribution at the $MoS_2$-to-metal interface, an energy-dispersive X-ray (EDX)−STEM analysis has been carried out along the stack, as indicated by the purple line in Figure 5c. The acquired data, plotted in Figure 5d, elucidate that the sulfur concentration is still considerable at the interface between $MoS_2$ and Ti, unlike the oxygen intensity that drops significantly beyond the $SiO_2$ substrate and remains only as the background. The latter is further clarified by providing the raw peak intensities in the Supporting Information (see Section S.6 and the associated discussion). The Mo profile, on the other hand, does not fall to zero, beyond the $MoS_2$-to-Ti interface. This is mainly because the sample is mounted on a Mo support grid. Therefore, the Mo background signal is unavoidably counted over the full range of the line scan. Altogether, the acquired elemental profiles suggest that $TiS_x$ is the most likely formed chemical compound on the $O_2$ plasma-cleaned $MoS_2$ surface, rather than $TiO_x$. Now, considering the vacuum pressure during the Ti/Au stack deposition in the e-beam evaporator, which is $\sim 4 \times 10^{-7}$ mbar, and the key role of the background oxygen in the chemical interactions at the metal-to-$MoS_2$ interface (discussed earlier), one can deduce that under near-UHV conditions, formation of $TiO_x$ is less probable. As a result, Ti tends to mostly react with S atoms of $MoS_2$,[35,36] forming an amorphous interlayer of about 2 nm in thickness. It is also important to point out that the formation of $MoO_3$ species during the $O_2$ plasma cleaning treatment and before the contact deposition (based on the XPS analysis) appears to be negligibly influencing the interface interactions because only a limited amount of oxygen (less than a monolayer) is detected by the XPS.

**Linking XPS and STEM to *I*−*V*.** Re-evaluating the measured *I*−*V* data and the extracted FE mobility (shown in Figure 3a,b), one could comprehensibly correlate the observed electrical behaviors with the $MoS_2$ surface chemical modifications, imposed by the plasma cleaning treatments. As concluded from the XPS analysis, both the Ar- and $O_2$ plasma cleaning treatments remove the organic residues from the $MoS_2$ surface up to some extent and alter the $MoS_2$ chemical state. The equally detected displacements in peak binding energies of both the Mo 3d and S 2p core level spectra reveal that $MoS_2$ $E_F$ is shifted further toward $E_c$ upon both plasma exposures. This could explain the observed improvements in the device on-state characteristics ($I_{on}$ and mobility), compared with when no cleaning treatment is employed on the $MoS_2$ surface (and the resist residual concentration remains significant), suggesting formation of less-impurity-interrupted contacts to $MoS_2$ upon the Ti/Au deposition. The cross-sectional STEM images in Figure 5a,b and the detection of an evenly distributed $TiS_x$ layer all along the Ti-to-$MoS_2$ interface (without a discontinuity) also verify the progress made in the contact quality upon the plasma cleaning treatments. Based on these investigations, conducted for the $O_2$ plasma-cleaned case, one could also infer that for the uncleaned $MoS_2$ surface, the organic resist residues may prevent the direct Ti reaction with the S atoms in $MoS_2$. The presence of these impurities may lead to the formation of lower-quality and discontinuous contacts to the underlying $MoS_2$, as also reported by Bolshakov et al.,[29] explaining the generally lower electrical performance, for the reference case, as compared with the plasma-cleaned counterparts.

Apart from the on-state performance enhancements, the observed $V_T$ negative shifts together with the dramatic increase in $I_{off}$ (in Figure 3a) could then be readily linked to the $MoS_2$ chemical changes and the shifts in the $E_F$ position, upon the cleaning treatments. Based on the XPS analysis, it was found that after the $O_2$ and Ar plasma exposures, $MoS_2$ $E_F$ shifts +0.5 eV and +0.2 eV closer to $E_c$, compared with when no plasma cleaning step is yet employed. Because the shift of $MoS_2$ $E_F$ (toward $E_c$) is larger for the $O_2$ plasma-treated sample, one would expect that the magnitude of $V_T$ increases and $I_{off}$ becomes higher for this case, compared with its Ar plasma-treated peer. However, a reverse behavior is observed. In other words, for the $O_2$ plasma-treated sample, $V_T$ shifts only −5 V with respect to the reference, and $I_{off}$ is 0.06 $\mu$A/$\mu$m, whereas for the Ar plasma-treated case, $\Delta V_T$ is −33 V and $I_{off}$ is 0.16 $\mu$A/$\mu$m. Elaborating the observations, it is important to note that the XPS analysis has been merely carried out before the metal contact deposition on the $MoS_2$ surface. After any metal deposition, $MoS_2$ $E_F$ is expected to move even closer to $E_c$,[29,34] with its magnitude being highly dependent on the degree of chemical interactions at the metal-to-$MoS_2$ interface. When the Ar plasma is applied on the $MoS_2$ surface, the concentration of metallic Mo and $Mo_xS_y$ increases (as confirmed by the XPS). Furthermore, the Ar plasma has proven to be more effective in removing the organic residues. As a result, once the Ti/Au contacts are deposited on the Ar plasma-cleaned $MoS_2$, the underlying $MoS_2$ is more degenerately doped, and its $E_F$ position is shifted closer to $E_c$, leading to more carrier injection and transport toward the $MoS_2$ channel, and thus higher $I_{off}$. Considering the $O_2$ plasma-treated sample and the difference in the nature of these two gases, the $MoS_2$ surface does not represent metallic Mo or $Mo_xS_y$ species. Therefore, after the contact deposition, it is speculated that the $MoS_2$ layer beneath Ti/Au is less excessively doped, leading to lower $I_{off}$ than in the case of Ar plasma treatment.

**Plasma Cleaning and Annealing of the $MoS_2$ Contacts.** With the purpose of further enhancing the device electrical characteristics, plasma cleaning together with the HV annealing treatments were also examined. Employing both treatments has their own benefits and drawbacks. We report that $I_{off}$ reduces,


https://doi.org/10.1021/acsaelm.1c00379
ACS Appl. Electron. Mater. 2021, 3, 3185−3199

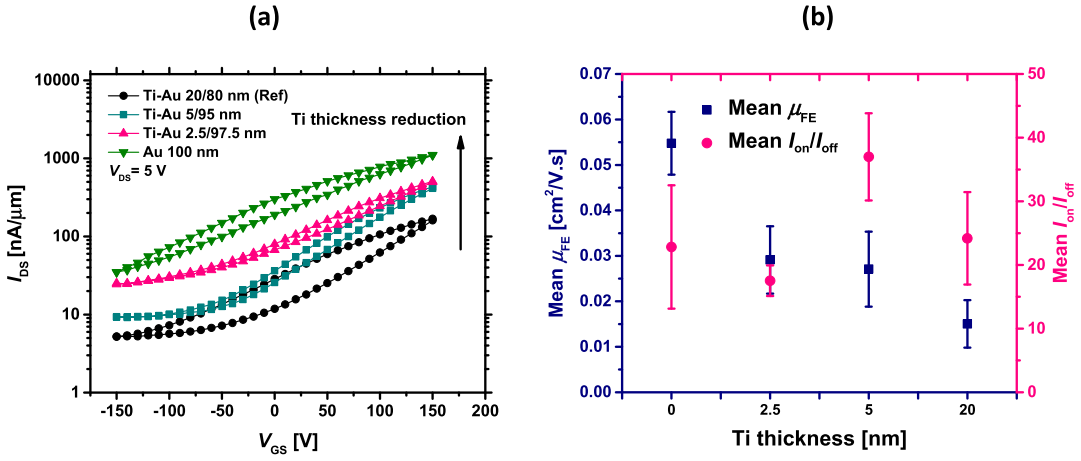


**Figure 6.** (a) Transfer curves of different Ti interlayer thicknesses, (b) average FE mobility at the left axis and the average $I_{on}/I_{off}$ ratio at the right axis as a function of reducing Ti thickness.

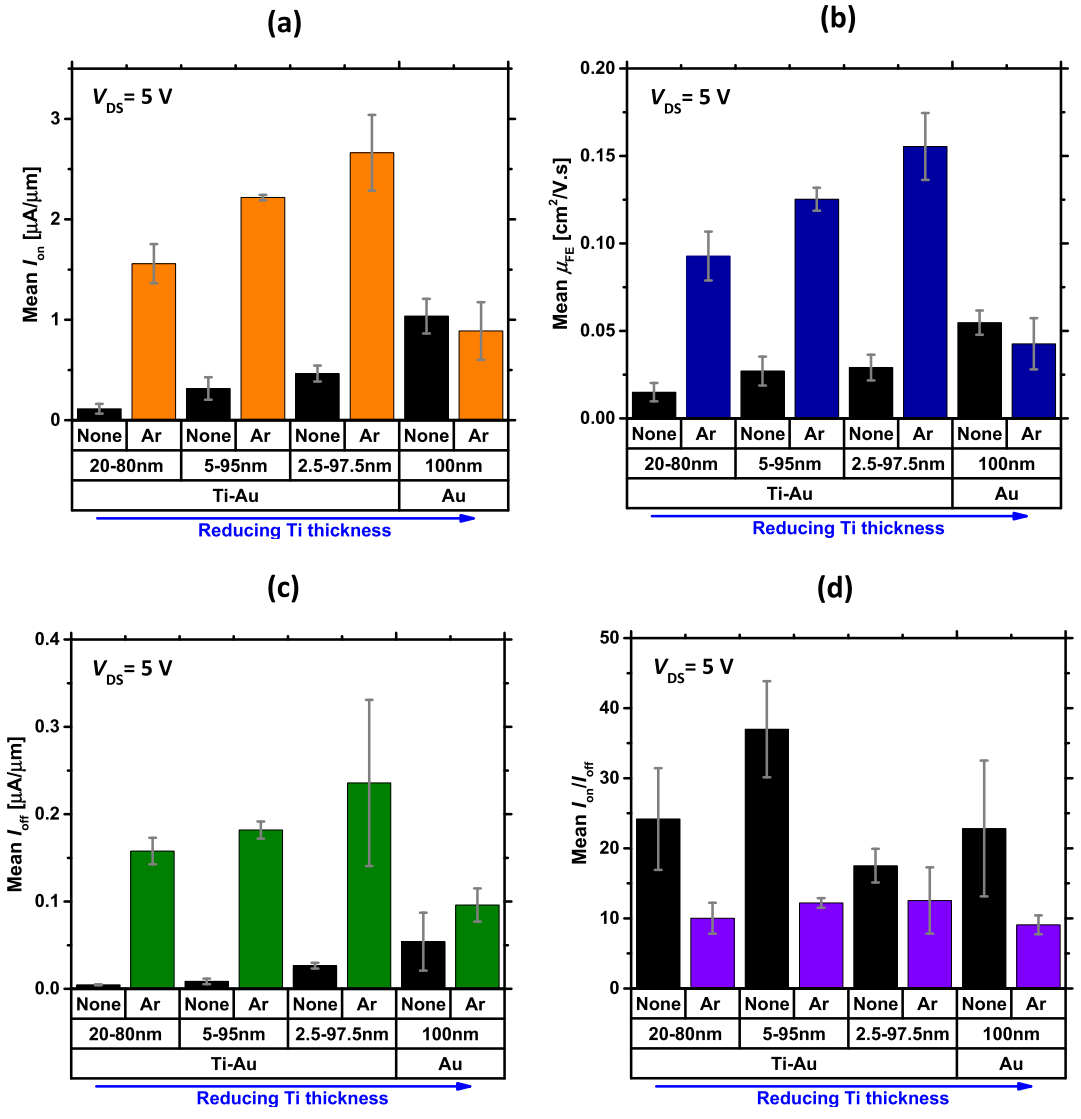


**Figure 7.** Average (a) $I_{on}$, (b) FE mobility, (c) $I_{off}$, and (d) $I_{on}/I_{off}$ ratio for the uncleaned and Ar plasma-cleaned contacts as a function of Ti interlayer thickness, respectively.

and $V_T$ shifts positively. Despite this progress in the off-state regime, $I_{on}$ and the FE mobility degrade, although the as-mentioned parameters are still better than when no cleaning treatment is applied. For further details, see Section S.7 in the Supporting Information and the associated discussion.



https://doi.org/10.1021/acsaelm.1c00379
ACS Appl. Electron. Mater. 2021, 3, 3185−3199

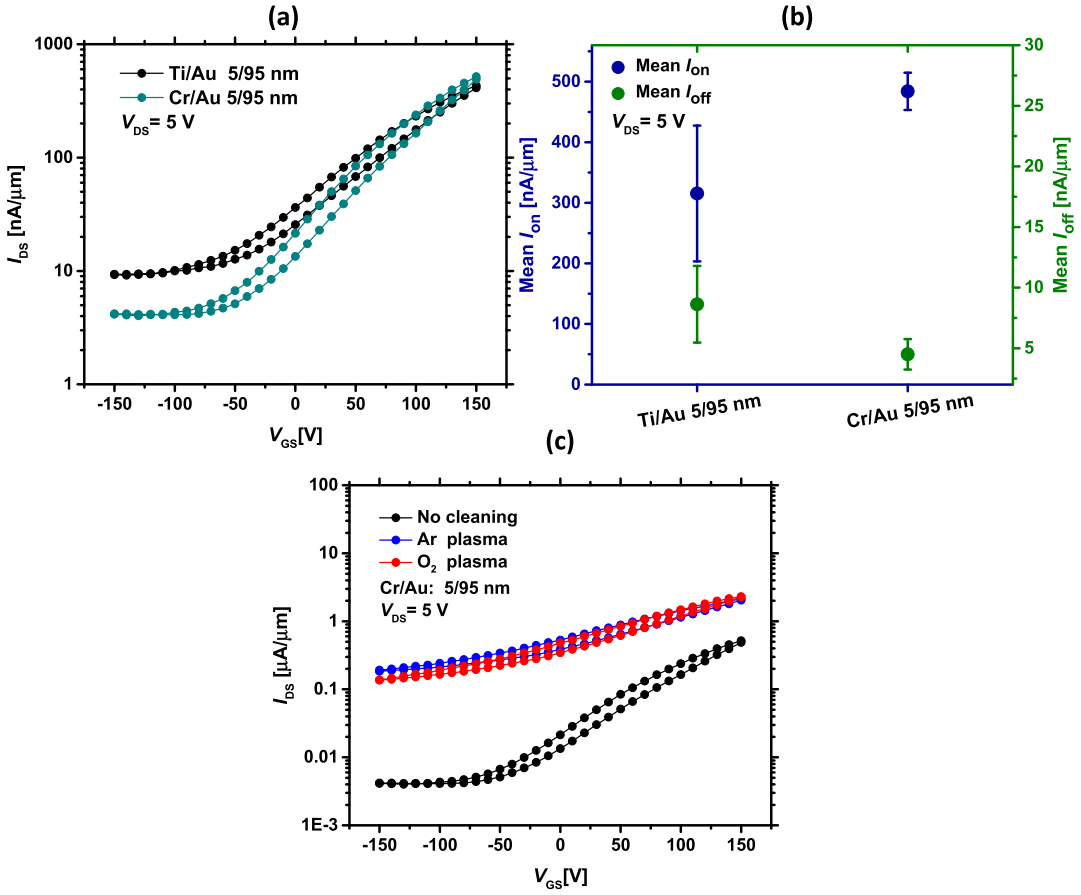


**Figure 8.** (a) Transfer curves of Cr/Au and Ti/Au 5/95 nm contacts, (b) Average $I_{on}$ (left axis) and average $I_{off}$ (right axis) for both contact types and (c) impact of plasma cleaning treatments before the Cr/Au deposition.

**Scaling Down the Ti Interlayer Thickness.** Up to this point, the Ti thickness has been maintained at 20 nm. Striving toward further optimizing the contacts for our ALD-based $MoS_2$ FETs, it is necessary to benchmark the influence of scaling down the Ti thickness on the overall device electrical performance. Ti is generally used as an adhesive interlayer between the $MoS_2$ and Au contacts. It is expected that reducing the Ti thickness facilitates the Au wavefunction penetration into the $MoS_2$, leading to further electrical improvements.[31] To verify this, various Ti thicknesses, ranging from 20 nm down to 2.5 nm, were examined, meanwhile maintaining the whole Ti/Au stack thickness at 100 nm. Complete removal of this interlayer was also inspected. Initially, no plasma cleaning treatment was employed to clean up the $MoS_2$ surface. Figure 6a shows the transfer curves of the fabricated $MoS_2$ FETs with Ti thickness variations. At first sight, it is explicit that upon the Ti thickness reduction, $I_{on}$ gradually increases and improves up to one order of magnitude, when Ti is completely removed from the contact stack (100 nm Au). On the other hand, $I_{off}$ deteriorates upon this reduction and $V_T$ shifts to more negative values, altogether implying that the $MoS_2$ gets further *n*-type doped. The increase in the $MoS_2$ doping concentration and the improvement in the device on-state performance are directly associated with further facileness of the Au wavefunction penetration into the $MoS_2$, as pointed earlier. This progress is also evident from the extracted FE mobilities, as shown in Figure 6b. On average, the maximum FE mobility increases about five times upon decreasing the Ti thickness and reaches nearly 0.06 $cm^2/(V{\cdot}s)$. The average mean $I_{on}/I_{off}$ ratio is also shown in this Figure, at its right axis. As can be seen, this ratio is maximum (about 40) when the Ti/Au stack is 5/95 nm, making this combination optimum as the contacts to $MoS_2$.

It is also of interest to gain insights into the impact of plasma cleaning treatment before the deposition of various Ti thicknesses. Figure 7a–d provides the average statistical data (on device figures of merit) for the Ar plasma-cleaned contact openings, as a function of Ti thickness and relative to their uncleaned peers. Excluding the pure Au contact analysis at first, the Ar plasma cleaning treatment significantly increases $I_{on}$, shown in Figure 7a. As earlier discussed, this is due to the improved quality of contacts to the $MoS_2$ and the continuous $TiS_x$ compound formation by adding the plasma cleaning step. The on-state performance is further continued to enhance with reducing the Ti thickness down to 2.5 nm. A similar trend is also observable in the extracted mean maximum FE mobilities, as provided in Figure 7b. Meanwhile, $I_{off}$ increases upon the plasma exposure, resulting in the $I_{on}/I_{off}$ ratio to fall below 20 for all the Ti thicknesses. The reason for such a dramatic increase in $I_{off}$ is attributed to the increase in the doping density, either because of extended Au wave function penetration with reducing the Ti thickness or formation of metallic Mo and $Mo_xS_y$ on the $MoS_2$ contact openings upon the Ar plasma cleaning treatment.

Considering the pure Au case, a deviating behavior is observed. Upon the Ar plasma cleaning treatment, $I_{on}$ as well as the FE mobility values slightly drop on average, whereas $I_{off}$ increases (Figure 7a–c, respectively), all compared to when no treatment is applied. It is already known from theoretical calculations that Au inclines to only weakly react with the surface


https://doi.org/10.1021/acsaelm.1c00379
ACS Appl. Electron. Mater. 2021, 3, 3185–3199

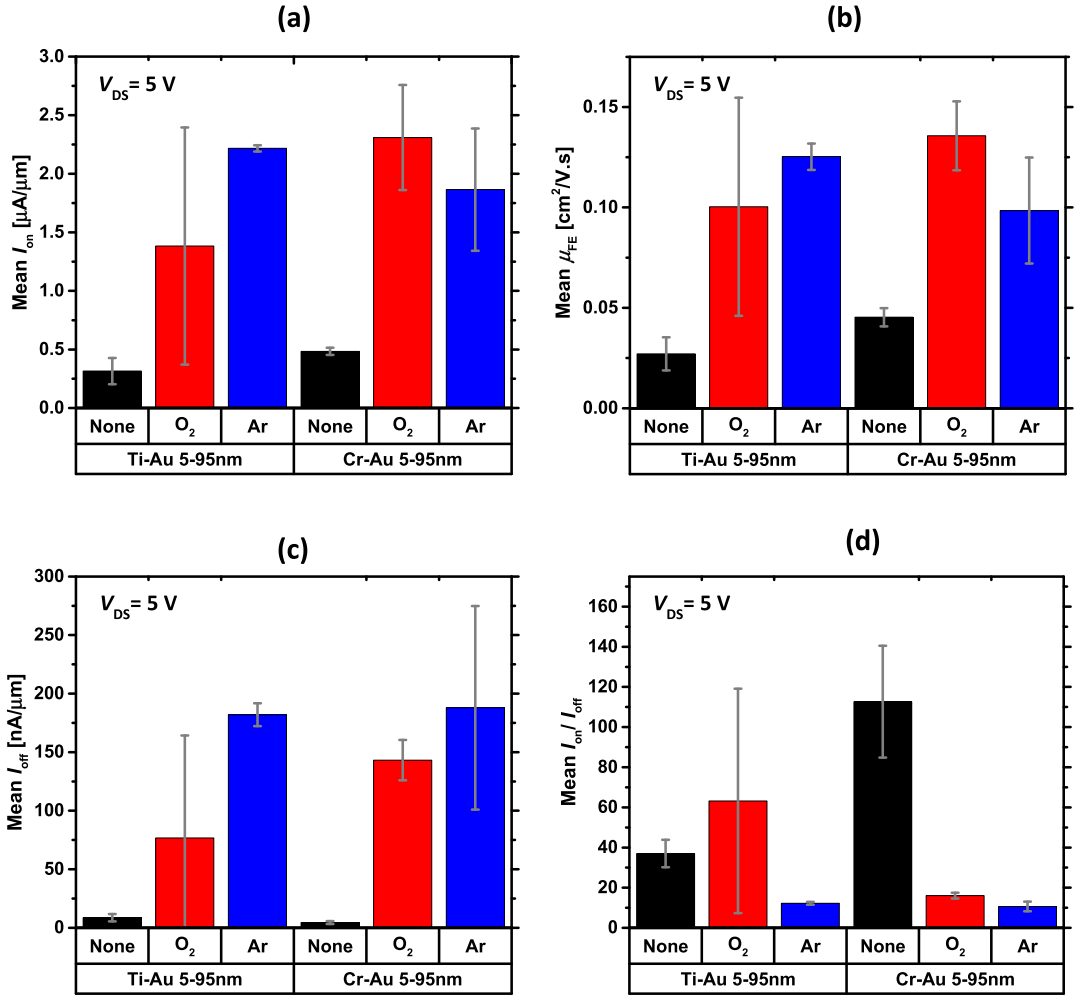


**Figure 9.** Benchmarking the 5/95 nm Cr/Au contacts with different plasma cleaning pretreatments comparative to Ti/Au. (a) Mean $I_{on}$, (b) mean FE mobility, (c) mean $I_{off}$ and (d) mean $I_{on}/I_{off}$, respectively.

of $MoS_2$ (unlike Ti that tends to form covalent bonds to this 2D layer), leaving behind an extra tunneling barrier against the efficient carrier injection at the interface. The tunneling barrier is in addition to the Schottky barrier and leads to higher $R_c$ values for $MoS_2$ FETs.[31] In our fabricated devices, however, as has been previously confirmed by the XPS data, the organic residual concentration on the $MoS_2$ surface is considerable when no plasma cleaning step is included. Therefore, it is speculated that the presence of surface impurities forms a bridge between Au and $MoS_2$ and lowers the interface tunneling barrier, leading to the observed improvements in the average $I_{on}$ and mobility (Figure 7a,b) of the devices (compared with the uncleaned Ti cases). On the other hand, application of the Ar plasma, prior to the pure Au deposition, results in a lower concentration of organic residues on the $MoS_2$ surface and likely an increase in the tunneling barrier. Thus, the on-state performance ($I_{on}$ and mobility) slightly drops on average and does not follow the trend observed for Ar plasma-cleaned Ti cases. In addition, based on the XPS data, the metallic Mo and $Mo_xS_y$ concentrations upon the Ar plasma cleaning process increase, causing the $MoS_2$ layer and its electronic band structure to disrupt, leading to an increase in $I_{off}$. Here, we note that the increase in $I_{off}$, after the Ar plasma treatment, does not follow the trend shown in Figure 7c, where $I_{off}$ increases up to one order of magnitude by decreasing the Ti thickness. This could still be associated with weaker interactions between the Au- and the plasma-cleaned $MoS_2$ surface, compared to when no adhesive interlayer is added. The transfer curves of the Au contacts with and without the Ar plasma cleaning treatment are provided in Figure S8 of the Supporting Information.

Analyzing the device electrical performance, for varied Ti thicknesses, reveals that among all the studied cases, the Ti/Au stack of 5/95 nm, without any Ar plasma cleaning treatment, is the optimal contact to our synthetic $MoS_2$ films. This is mainly because the $I_{on}/I_{off}$ ratio, as one of the other important device figures of merit, is the highest when 5 nm of the Ti interlayer is deposited.

**Substitution of the Ti Interlayer with Cr.** Continuing the optimization path of the contacts for the ALD-based $MoS_2$ FETs, the 5 nm Ti interlayer was replaced with 5 nm of Cr, meanwhile the metal deposition conditions (e.g., pressure and deposition rate) were kept constant. Initially, no plasma cleaning treatment was employed. The reason for choosing Cr is that Cr is known to have a lower affinity for oxidation, compared with Ti.[34,35] Therefore, it is expected that its interaction with the organic contaminations as well as the underlying $MoS_2$ surface is relatively weaker. The schematics of the energy band diagrams before and after the contact deposition on $MoS_2$, for both cases, are provided in the Supporting Information (Section S.9). The transfer curves of the $MoS_2$ FETs with Cr and Ti interlayers are


https://doi.org/10.1021/acsaelm.1c00379
ACS Appl. Electron. Mater. 2021, 3, 3185−3199

compared in Figure 8a. As can be seen from the plot, utilization of Cr instead of Ti leads to better controlling $I_{off}$ and improving $I_{on}$, suggesting that the degree of $MoS_2$ doping and its electronic band structure disruption is mitigated with the Cr substitution. This is first because the Cr−S formation energy is higher than that of Ti−S, and both are lower than that of Mo−S, based on the Gibbs free energy of formation ($\Delta G^{o}_{f}$).[34,35] $\Delta G^{o}_{f}$ for $Cr_2S_3$ is −148.19 kJ/mol, for $TiS_x$ it is in the range of −573 to −390 kJ/mol, depending on $x$, and for $MoS_2$ it is −117.99 kJ/m.[34,35] These values clearly indicate that Ti−S formation is more favorable than Cr−S. Second, the electronegativity difference between Cr−S is lower than that of Ti−S, implying that Cr−S bonds are weaker than Ti−S bonds, and the degree of $MoS_2$ disruption is lower in the case of Cr contacts. In addition, Cr is not expected to react with the residual components as strongly as in the case of Ti (Cr−C and Cr−O electronegativity differences are less than those of Ti−C and Ti−O). As a result, on average, $I_{off}$ for the Cr/Au stack drops to half of the value obtained from Ti/Au, and $I_{on}$ increases 1.5 fold, as evident in Figure 8b on the right and left axes, respectively.

Inclusion of the plasma cleaning step for the Cr contacts and its impact on the electrical performance are also evaluated. Figure 8c compares the measured transfer data for the Ar and $O_2$ plasma-treated $MoS_2$ FETs, with respect to the uncleaned reference. Analogous to the Ti/Au cases, addition of the plasma cleaning step improves the device on-state features ($I_{on}$ and the mobility), while the off-state performance deteriorates because $MoS_2$ becomes degenerately doped and the back gate fails to efficiently deplete the channel, leading to a significant increase in $I_{off}$ and a significant negative shift in $V_T$.

The average overall electrical characteristics of the fabricated $MoS_2$ devices with both types of metal contacts are also evaluated. As can be seen from Figure 9a,b, substitution of Ti with Cr (without any initial plasma cleaning) doubles the mean $I_{on}$ and FE mobility values. Although this improvement might be minor, the mean $I_{off}$ for the Cr/Au stack decreases as well (see Figure 9c). As a result, the $I_{on}/I_{off}$ ratio, provided in Figure 9d, improves on average and reaches ∼110. These assessments on the overall electrical characteristics of the fabricated $MoS_2$ devices, with both types of contacts, reveal that the plasma cleaning treatments are beneficial in improving the device on-state performance. However, due to the lack of gate electrostatic control over the off-state current, the noncleaned devices are performing more optimally than their plasma-cleaned counterparts. One way to control $I_{off}$ is to thin down the $MoS_2$ thickness, which will be discussed in a forthcoming paper. Among the two studied interlayers, Cr exhibits a better performance than Ti, as a result of its higher $I_{on}/I_{off}$ ratio.

All in all, the provided results and the associated discussions lead to better recognizing the chemistry involved at the metal-to-synthetic $MoS_2$ interfaces and their direct influence on the overall device electrical performance.

## CONCLUSIONS

In this study, working ALD-based $MoS_2$ FETs have been successfully demonstrated, and the role of device processing conditions in the chemistry involved at the metal-to-$MoS_2$ interface as well as their correlation with the electrical performance have been investigated in detail. This work highlights that understanding and tailoring the device-processing conditions as well as the contacts to $MoS_2$ are vital for achieving optimal electrical performance, especially for the synthetic $MoS_2$ films, where the role of intrinsic and process-induced defects in transport properties is even more pronounced than for their exfoliated counterparts.

In pursuit of optimizing the contacts to our $MoS_2$ FETs, several efforts have been made. These are HV annealing the contacts after their deposition, plasma cleaning the contact opening areas and scaling down the Ti interlayer thickness as well as its substitution with Cr.

We have shown that annealing the Ti/Au contacts to $MoS_2$, in a HV environment, is not effective in improving the on-state device performance. However, $V_T$ shifts positively and $I_{off}$ lowers, indicating that upon the Ti/Au HV annealing, $MoS_2$ becomes relatively less $n$-type doped.

Furthermore, inclusion of the $O_2$ or Ar plasma cleaning step (prior to the contact deposition) enhances the device on-state characteristics, up to one order of magnitude. This is while $I_{off}$ deteriorates, due to $MoS_2$ being degenerately doped. For linking the role of interface chemistry to the electrical observations, XPS and STEM analyses have been conducted. The XPS study reveals that the impurity concentration on the $MoS_2$ contact opening areas is significant. This is the result of resist usage during the device fabrication that could hinder the utmost performance, being achieved from our fabricated devices. The analysis also shows that addition of a mild plasma cleaning step removes a considerable portion of the resist remainders and shifts the $MoS_2$ $E_F$ position closer to $E_c$, all of which are directly associated with the observed improvements in the device on-state performance. Apart from the surface impurity reduction, the electrical progress in our fabricated $MoS_2$ FETs is also attributed to the formation of an evenly distributed and continuous $TiS_x$ layer, all along the $MoS_2$ surface and upon the Ti deposition, as confirmed by the STEM analysis.

Scaling down the Ti interlayer thickness is proved to be necessary as well, for further unleashing the capability of our $MoS_2$ films and for being possibly implemented in transistor platforms.

In the last attempt, the replacement of the Ti interlayer with Cr, in the contact stack, has been evaluated. The results show that upon the Cr usage, the gate electrostatic control over the off-state current improves, meanwhile the $I_{on}$ range retains.

## ASSOCIATED CONTENT

### Supporting Information

The Supporting Information is available free of charge at https://pubs.acs.org/doi/10.1021/acsaelm.1c00379.

> Lay out of fabricated $MoS_2$ FETs; extraction of $V_T$ in $MoS_2$ FETs with the Y-function method; FE mobility extraction; O 1s and C 1s spectra of the as-synthesized $MoS_2$ films; Mo 3d and S 2p spectra after the PMMA pattern development; EDX−STEM raw and semi-quantitative data; impact of annealing the $O_2$ plasma-treated contacts; Ar plasma cleaning of the opening areas before the pure Au deposition; substitution of Ti/Au contacts with Cr/Au and the band diagrams (PDF)

## AUTHOR INFORMATION

### Corresponding Author

**Ageeth A. Bol** − *Department of Applied Physics, Eindhoven University of Technology, Eindhoven 5600 MB, The Netherlands;* orcid.org/0000-0002-1259-6265; Email: a.a.bol@tue.nl

## Authors

**Reyhaneh Mahlouji** − *Department of Applied Physics, Eindhoven University of Technology, Eindhoven 5600 MB, The Netherlands*

**Yue Zhang** − *Laboratory of Inorganic Materials and Catalysis, Department of Chemical Engineering and Chemistry, Eindhoven University of Technology, Eindhoven 5600 MB, The Netherlands*

**Marcel A. Verheijen** − *Department of Applied Physics, Eindhoven University of Technology, Eindhoven 5600 MB, The Netherlands; Eurofins Materials Science, Eindhoven 5656 AE, The Netherlands;* orcid.org/0000-0002-8749-7755

**Jan P. Hofmann** − *Laboratory of Inorganic Materials and Catalysis, Department of Chemical Engineering and Chemistry, Eindhoven University of Technology, Eindhoven 5600 MB, The Netherlands; Surface Science Laboratory, Department of Materials and Earth Sciences, Technical University of Darmstadt, Darmstadt 64287, Germany;* orcid.org/0000-0002-5765-1096

**Wilhelmus M. M. Kessels** − *Department of Applied Physics, Eindhoven University of Technology, Eindhoven 5600 MB, The Netherlands;* orcid.org/0000-0002-7630-8226

**Abhay A. Sagade** − *Laboratory for Advanced Nanoelectronic Devices, Department of Physics and Nanotechnology, SRM Institute of Science and Technology, Kattankulathur 603 203, Tamil Nadu, India*

Complete contact information is available at: https://pubs.acs.org/10.1021/acsaelm.1c00379


## Author Contributions

R.M conducted the experiments and wrote the manuscript, R.M grew the $MoO_x$ films and Y.Z sulfurized them, R.M fabricated the $MoS_2$ FETs and electrically/chemically characterized them, and M.A.V. performed the STEM and EDX analyses. All the authors approved the final version of the manuscript.

## Notes

The authors declare no competing financial interest.

## ■ ACKNOWLEDGMENTS

This work was funded by the European research council (ERC) under the grant Agreement no. 648787-ALDof2DTMDs. The authors would like to acknowledge the NanoLab@TU/e for the cleanroom facilities and the technical support of E. J. Geluk, E. Smalbrugge, T. de Vries, C. V. Helvoirt, M. G. Dijstelbloem, J. V. Gerwen, W. M. Dijkstra, and J. J. A. Zeebregts. Furthermore, the work of Dr. B. Barcones Campo for the cross-sectional STEM sample preparation with the FIB is gratefully appreciated. R.M. would like to also express her gratitude to E. J. Geluk, Dr. M.H. Diniz Guimaraes, Dr. N. F. W. Thissen, Dr. A. Sharma, Dr. S. Karwal and Dr. K. Ramezanpour for the useful scientific and practical discussions and Molecular Materials and Nanosystems (M2N) research group for supplying resources to conduct the electrical measurements as well as the advanced nanomaterials and devices (AND) group for providing access to their glovebox sample storage. Finally, Solliance and the Dutch province of Noord Brabant are acknowledged for funding the TEM facility.

## ■ REFERENCES


(1) Cao, W.; Kang, J.; Sarkar, D.; Liu, W.; Banerjee, K. Performance Evaluation and Design Considerations of 2D Semiconductor Based FETs for Sub-10 Nm VLSI. *2014 IEEE International Electron Devices Meeting*; IEEE, 2014; Vol. *2015*, pp 30.5.1−30.5.4.

(2) Cao, W.; Kang, J.; Sarkar, D.; Liu, W.; Banerjee, K. 2D Semiconductor FETs—Projections and Design for Sub-10 Nm VLSI. *IEEE Trans. Electron Devices* **2015**, *62*, 3459−3469.

(3) Cao, W.; Liu, W.; Banerjee, K. Prospects of Ultra-Thin Nanowire Gated 2D-FETs for next-Generation CMOS Technology. *2016 IEEE International Electron Devices Meeting (IEDM)*; IEEE, 2016; pp 14.7.1−14.7.4.

(4) Wang, Q. H.; Kalantar-Zadeh, K.; Kis, A.; Coleman, J. N.; Strano, M. S. Electronics and Optoelectronics of Two-Dimensional Transition Metal Dichalcogenides. *Nat. Nanotechnol.* **2012**, *7*, 699−712.

(5) Manzeli, S.; Ovchinnikov, D.; Pasquier, D.; Yazyev, O. V.; Kis, A. 2D Transition Metal Dichalcogenides. *Nat. Rev. Mater.* **2017**, *2*, 17033.

(6) Li, W.; Zhou, J.; Cai, S.; Yu, Z.; Zhang, J.; Fang, N.; Li, T.; Wu, Y.; Chen, T.; Xie, X.; Ma, H.; Yan, K.; Dai, N.; Wu, X.; Zhao, H.; Wang, Z.; He, D.; Pan, L.; Shi, Y.; Wang, P.; Chen, W.; Nagashio, K.; Duan, X.; Wang, X. Uniform and Ultrathin High-$\kappa$ Gate Dielectrics for Two-Dimensional Electronic Devices. *Nat. Electron.* **2019**, *2*, 563−571.

(7) Radisavljevic, B.; Radenovic, A.; Brivio, J.; Giacometti, V.; Kis, A. Single-Layer $MoS_2$ Transistors. *Nat. Nanotechnol.* **2011**, *6*, 147−150.

(8) Illarionov, Y. Y.; Smithe, K. K. H.; Waltl, M.; Knobloch, T.; Pop, E.; Grasser, T. Improved Hysteresis and Reliability of $MoS_2$ Transistors With High-Quality CVD Growth and Al2O3 Encapsulation. *IEEE Electron Device Lett.* **2017**, *38*, 1763−1766.

(9) Leonhardt, A.; Chiappe, D.; Afanas'ev, V. V.; El Kazzi, S.; Shlyakhov, I.; Conard, T.; Franquet, A.; Huyghebaert, C.; de Gendt, S. Material-Selective Doping of 2D TMDC through $Al_xO_y$ Encapsulation. *ACS Appl. Mater. Interfaces* **2019**, *11*, 42697−42707.

(10) Kang, K.; Xie, S.; Huang, L.; Han, Y.; Huang, P. Y.; Mak, K. F.; Kim, C.-J.; Muller, D.; Park, J. High-Mobility Three-Atom-Thick Semiconducting Films with Wafer-Scale Homogeneity. *Nature* **2015**, *520*, 656−660.

(11) Bertolazzi, S.; Brivio, J.; Kis, A. Stretching and Breaking of Ultrathin $MoS_2$. *ACS Nano* **2011**, *5*, 9703−9709.

(12) Cheng, R.; Jiang, S.; Chen, Y.; Liu, Y.; Weiss, N.; Cheng, H.-C.; Wu, H.; Huang, Y.; Duan, X. Few-Layer Molybdenum Disulfide Transistors and Circuits for High-Speed Flexible Electronics. *Nat. Commun.* **2014**, *5*, 5143.

(13) Smithe, K. K. H.; Suryavanshi, S. V.; Muñoz Rojo, M.; Tedjarati, A. D.; Pop, E. Low Variability in Synthetic Monolayer MoS2 Devices. *ACS Nano* **2017**, *11*, 8456−8463.

(14) Radisavljevic, B.; Whitwick, M. B.; Kis, A. Integrated Circuits and Logic Operations Based on Single-Layer $MoS_2$. *ACS Nano* **2011**, *5*, 9934−9938.

(15) Wachter, S.; Polyushkin, D. K.; Bethge, O.; Mueller, T. A Microprocessor Based on a Two-Dimensional Semiconductor. *Nat. Commun.* **2017**, *8*, 14948.

(16) Huyghebaert, C.; Schram, T.; Smets, Q.; Kumar Agarwal, T.; Verreck, D.; Brems, S.; Phommahaxay, A.; Chiappe, D.; El Kazzi, S.; Lockhart de la Rosa, C.; Arutchelvan, G.; Cott, D.; Ludwig, J.; Gaur, A.; Sutar, S.; Leonhardt, A.; Marinov, D.; Lin, D.; Caymax, M.; Asselberghs, I.; Pourtois, G.; Radu, I. P. 2D Materials: Roadmap to CMOS Integration. *2018 IEEE International Electron Devices Meeting (IEDM)*; IEEE, 2018; Vol. *2018*, pp 22.1.1−22.1.4. DOI: 10.1109/IEDM.2018.8614679.

(17) Appenzeller, J.; Zhang, F.; Das, S.; Knoch, J. Transition Metal Dichalcogenide Schottky Barrier Transistors. *2D Materials for Nanoelectronics*; Taylor & Francis Group, LLC: Boca Raton, FL, 2016; pp 207−240.

(18) Chhowalla, M.; Jena, D.; Zhang, H. Two-Dimensional Semiconductors for Transistors. *Nat. Rev. Mater.* **2016**, *1*, 16052.

(19) Allain, A.; Kang, J.; Banerjee, K.; Kis, A. Electrical Contacts to Two-Dimensional Semiconductors. *Nat. Mater.* **2015**, *14*, 1195−1205.

(20) Sze, S. M. *Semiconductor Devices Physics and Technology*; Wiley: New York, N.Y., 2002.

(21) Chuang, H.-J.; Chamlagain, B.; Koehler, M.; Perera, M. M.; Yan, J.; Mandrus, D.; Tománek, D.; Zhou, Z. Low-Resistance 2D/2D Ohmic Contacts: A Universal Approach to High-Performance $WSe_2$, $MoS_2$, and $MoSe_2$ Transistors. *Nano Lett.* **2016**, *16*, 1896−1902.

(22) Heo, K.; Jo, S.-H.; Shim, J.; Kang, D.-H.; Kim, J.-H.; Park, J.-H. Stable and Reversible Triphenylphosphine-Based n-Type Doping Technique for Molybdenum Disulfide ($MoS_2$). *ACS Appl. Mater. Interfaces* **2018**, *10*, 32765−32772.
(23) Tung, R. T. Chemical Bonding and Fermi Level Pinning at Metal-Semiconductor Interfaces. *Phys. Rev. Lett.* **2000**, *84*, 6078−6081.
(24) Das, S.; Chen, H.-Y.; Penumatcha, A. V.; Appenzeller, J. High Performance Multilayer $MoS_2$ Transistors with Scandium Contacts. *Nano Lett.* **2013**, *13*, 100−105.
(25) Kim, C.; Moon, I.; Lee, D.; Choi, M. S.; Ahmed, F.; Nam, S.; Cho, Y.; Shin, H.-J.; Park, S.; Yoo, W. J. Fermi Level Pinning at Electrical Metal Contacts of Monolayer Molybdenum Dichalcogenides. *ACS Nano* **2017**, *11*, 1588−1596.
(26) Gong, C.; Colombo, L.; Wallace, R. M.; Cho, K. The Unusual Mechanism of Partial Fermi Level Pinning at Metal−$MoS_2$ Interfaces. *Nano Lett.* **2014**, *14*, 1714−1720.
(27) Zhou, W.; Zou, X.; Najmaei, S.; Liu, Z.; Shi, Y.; Kong, J.; Lou, J.; Ajayan, P. M.; Yakobson, B. I.; Idrobo, J.-C. Intrinsic Structural Defects in Monolayer Molybdenum Disulfide. *Nano Lett.* **2013**, *13*, 2615−2622.
(28) Najmaei, S.; Yuan, J.; Zhang, J.; Ajayan, P.; Lou, J. Synthesis and Defect Investigation of Two-Dimensional Molybdenum Disulfide Atomic Layers. *Acc. Chem. Res.* **2015**, *48*, 31−40.
(29) Bolshakov, P.; Smyth, C. M.; Khosravi, A.; Zhao, P.; Hurley, P. K.; Hinkle, C. L.; Wallace, R. M.; Young, C. D. Contact Engineering for Dual-Gate $MoS_2$ Transistors Using $O_2$ Plasma Exposure. *ACS Appl. Electron. Mater.* **2019**, *1*, 210−219.
(30) Schauble, K.; Zakhidov, D.; Yalon, E.; Deshmukh, S.; Grady, R. W.; Cooley, K. A.; McClellan, C. J.; Vaziri, S.; Passarello, D.; Mohney, S. E.; Toney, M. F.; Sood, A. K.; Salleo, A.; Pop, E. Uncovering the Effects of Metal Contacts on Monolayer $MoS_2$. *ACS Nano* **2020**, *14*, 14798−14808.
(31) Kang, J.; Liu, W.; Sarkar, D.; Jena, D.; Banerjee, K. Computational Study of Metal Contacts to Monolayer Transition-Metal Dichalcogenide Semiconductors. *Phys. Rev. X* **2014**, *4*, 031005.
(32) Luo, B.; Liu, J.; Zhu, S. C.; Yi, L. Chromium is Proposed as an Ideal Metal to Form Contacts with Monolayer $MoS_2$ and $WS_2$. *Mater. Res. Express* **2015**, *2*, 106501.
(33) Luo, Y.-R. *Comprehensive Handbook of Chemical Bond Energies*; CRC Press, 2007.
(34) Smyth, C. M.; Addou, R.; McDonnell, S.; Hinkle, C. L.; Wallace, R. M. Contact Metal−$MoS_2$ Interfacial Reactions and Potential Implications on $MoS_2$ -Based Device Performance. *J. Phys. Chem. C* **2016**, *120*, 14719−14729.
(35) McDonnell, S.; Smyth, C.; Hinkle, C. L.; Wallace, R. M. $MoS_2$—Titanium Contact Interface Reactions. *ACS Appl. Mater. Interfaces* **2016**, *8*, 8289−8294.
(36) Wu, R. J.; Udyavara, S.; Ma, R.; Wang, Y.; Chhowalla, M.; Birol, T.; Koester, S. J.; Neurock, M.; Mkhoyan, K. A. Visualizing the Metal-$MoS_2$ Contacts in Two-Dimensional Field-Effect Transistors with Atomic Resolution. *Phys. Rev. Mater.* **2019**, *3*, 111001.
(37) Lee, S.; Tang, A.; Aloni, S.; Philip Wong, H.-S. Statistical Study on the Schottky Barrier Reduction of Tunneling Contacts to CVD Synthesized $MoS_2$. *Nano Lett.* **2016**, *16*, 276−281.
(38) Park, W.; Kim, Y.; Lee, S. K.; Jung, U.; Yang, J. H.; Cho, C.; Kim, Y. J.; Lim, S. K.; Hwang, I. S.; Lee, H.-B.-R.; Lee, B. H. Contact Resistance Reduction Using Fermi Level De-Pinning Layer for $MoS_2$ FETs. *2014 IEEE International Electron Devices Meeting*; IEEE, 2014; Vol. *2015*, pp 5.1.1−5.1.4.
(39) Kim, G.-S.; Kim, S.-H.; Park, J.; Han, K. H.; Kim, J.; Yu, H.-Y. Schottky Barrier Height Engineering for Electrical Contacts of Multilayered $MoS_2$ Transistors with Reduction of Metal-Induced Gap States. *ACS Nano* **2018**, *12*, 6292−6300.
(40) Islam, M. R.; Kang, N.; Bhanu, U.; Paudel, H. P.; Erementchouk, M.; Tetard, L.; Leuenberger, M. N.; Khondaker, S. I. Tuning the Electrical Property via Defect Engineering of Single Layer $MoS_2$ by Oxygen Plasma. *Nanoscale* **2014**, *6*, 10033.
(41) Marinov, D.; de Marneffe, J.-F.; Smets, Q.; Arutchelvan, G.; Bal, K. M.; Voronina, E.; Rakhimova, T.; Mankelevich, Y.; El Kazzi, S.; Nalin Mehta, A.; Wyndaele, P.-J.; Heyne, M. H.; Zhang, J.; With, P. C.; Banerjee, S.; Neyts, E. C.; Asselberghs, I.; Lin, D.; De Gendt, S. Reactive Plasma Cleaning and Restoration of Transition Metal Dichalcogenide Monolayers. *npj 2D Mater. Appl.* **2021**, *5*, 17.
(42) English, C. D.; Shine, G.; Dorgan, V. E.; Saraswat, K. C.; Pop, E. Improved Contacts to $MoS_2$ Transistors by Ultra-High Vacuum Metal Deposition. *Nano Lett.* **2016**, *16*, 3824−3830.
(43) Abraham, M.; Mohney, S. E. Annealed Ag Contacts to $MoS_2$ Field-Effect Transistors. *J. Appl. Phys.* **2017**, *122*, 115306.
(44) Zhao, P.; Azcatl, A.; Bolshakov, P.; Moon, J.; Hinkle, C. L.; Hurley, P. K.; Wallace, R. M.; Young, C. D. Effects of Annealing on Top-Gated $MoS_2$ Transistors with $HfO_2$ Dielectric. *J. Vac. Sci. Technol., B: Nanotechnol. Microelectron.: Mater., Process., Meas., Phenom.* **2017**, *35*, 01A118.
(45) Lee, Y.-H.; Zhang, X.-Q.; Zhang, W.; Chang, M.-T.; Lin, C.-T.; Chang, K.-D.; Yu, Y.-C.; Wang, J. T.-W.; Chang, C.-S.; Li, L.-J.; Lin, T.-W. Synthesis of Large-Area $MoS_2$ Atomic Layers with Chemical Vapor Deposition. *Adv. Mater.* **2012**, *24*, 2320−2325.
(46) Zhao, Y.; Jin, S. Controllable Water Vapor Assisted Chemical Vapor Transport Synthesis of $WS_2$−$MoS_2$ Heterostructure. *ACS Mater. Lett.* **2020**, *2*, 42−48.
(47) Tian, Z.-L.; Zhao, D.-H.; Liu, H.; Zhu, H.; Chen, L.; Sun, Q.-Q.; Zhang, D. W. Optimization of Defects in Large-Area Synthetic $MoS_2$ Thin Films by $CS_2$ Treatment for Switching and Sensing Devices. *ACS Appl. Nano Mater.* **2019**, *2*, 7810−7818.
(48) Jeon, W.; Cho, Y.; Jo, S.; Ahn, J. H.; Jeong, S. J. Wafer-Scale Synthesis of Reliable High-Mobility Molybdenum Disulfide Thin Films via Inhibitor-Utilizing Atomic Layer Deposition. *Adv. Mater.* **2017**, *29*, 1−8.
(49) Sharma, A.; Verheijen, M. A.; Wu, L.; Karwal, S.; Vandalon, V.; Knoops, H. C. M.; Sundaram, R. S.; Hofmann, J. P.; Erwin Kessels, W. M. M.; Bol, A. A. Low-Temperature Plasma-Enhanced Atomic Layer Deposition of 2-D $MoS_2$: Large Area, Thickness Control and Tuneable Morphology. *Nanoscale* **2018**, *10*, 8615−8627.
(50) Pyeon, J. J.; Baek, I.-H.; Lim, W. C.; Chae, K. H.; Han, S. H.; Lee, G. Y.; Baek, S.-H.; Kim, J.-S.; Choi, J.-W.; Chung, T.-M.; Han, J. H.; Kang, C.-Y.; Kim, S. K. Low-Temperature Wafer-Scale Synthesis of Two-Dimensional $SnS_2$. *Nanoscale* **2018**, *10*, 17712−17721.
(51) Sharma, A.; Mahlouji, R.; Wu, L.; Verheijen, M. A.; Vandalon, V.; Balasubramanyam, S.; Hofmann, J. P.; Erwin Kessels, W. M. M.; Bol, A. A. Large Area, Patterned Growth of 2D $MoS_2$ and Lateral $MoS_2$-$WS_2$ Heterostructures for Nano- and Opto-Electronic Applications. *Nanotechnology* **2020**, *31*, 255603.
(52) Sharma, A.; Longo, V.; Verheijen, M. A.; Bol, A. A.; Erwin Kessels, W. M. M. Atomic Layer Deposition of $HfO_2$ Using $HfCp(NMe_2)_3$ and $O_2$ Plasma. *J. Vac. Sci. Technol., A* **2017**, *35*, 01B130.
(53) Jena, D.; Konar, A. Enhancement of Carrier Mobility in Semiconductor Nanostructures by Dielectric Engineering. *Phys. Rev. Lett.* **2007**, *98*, 136805.
(54) Valsaraj, A.; Chang, J.; Rai, A.; Register, L. F.; Banerjee, S. K. Theoretical and Experimental Investigation of Vacancy-Based Doping of Monolayer $MoS_2$ on Oxide. *2D Mater.* **2015**, *2*, 045009.
(55) McClellan, C. J.; Yalon, E.; Smithe, K. K. H.; Suryavanshi, S. V.; Pop, E. High Current Density in Monolayer $MoS_2$ Doped by $AlO_x$. *ACS Nano* **2021**, *15*, 1587−1596.
(56) Leong, W. S.; Li, Y.; Luo, X.; Nai, C. T.; Quek, S. Y.; Thong, J. T. L. Tuning the Threshold Voltage of $MoS_2$ Field-Effect Transistors via Surface Treatment. *Nanoscale* **2015**, *7*, 10823−10831.
(57) Du, H.; Kim, T.; Shin, S.; Kim, D.; Kim, H.; Sung, J. H.; Lee, M. J.; Seo, D. H.; Lee, S. W.; Jo, M.-H.; Seo, S. Schottky Barrier Contrasts in Single and Bi-Layer Graphene Contacts for $MoS_2$ Field-Effect Transistors. *Appl. Phys. Lett.* **2015**, *107*, 233106.
(58) Pak, J.; Cho, K.; Kim, J.-K.; Jang, Y.; Shin, J.; Kim, J.; Seo, J.; Chung, S.; Lee, T. Trapped Charge Modulation at the $MoS_2/SiO_2$ Interface by a Lateral Electric Field in $MoS_2$ Field-Effect Transistors. *Nano Futures* **2019**, *3*, 011002.
(59) Freedy, K. M.; Zhang, H.; Litwin, P. M.; Bendersky, L. A.; Davydov, A. V.; McDonnell, S. Thermal Stability of Titanium Contacts to $MoS_2$. *ACS Appl. Mater. Interfaces* **2019**, *11*, 35389−35393.

(60) Chang, H.-Y.; Zhu, W.; Akinwande, D. On the Mobility and Contact Resistance Evaluation for Transistors Based on $MoS_2$ or Two-Dimensional Semiconducting Atomic Crystals. *Appl. Phys. Lett.* **2014**, *104*, 113504.
(61) McDonnell, S.; Addou, R.; Buie, C.; Wallace, R. M.; Hinkle, C. L. Defect-Dominated Doping and Contact Resistance in $MoS_2$. *ACS Nano* **2014**, *8*, 2880−2888.
(62) Kim, I. S.; Sangwan, V. K.; Jariwala, D.; Wood, J. D.; Park, S.; Chen, K.-S.; Shi, F.; Ruiz-Zepeda, F.; Ponce, A.; Jose-Yacaman, M.; Dravid, V. P.; Marks, T. J.; Hersam, M. C.; Lauhon, L. J. Influence of Stoichiometry on the Optical and Electrical Properties of Chemical Vapor Deposition Derived $MoS_2$. *ACS Nano* **2014**, *8*, 10551−10558.



https://doi.org/10.1021/acsaelm.1c00379
*ACS Appl. Electron. Mater.* 2021, 3, 3185−3199